THE UNIVERSITY *of* EDINBURGH
School of Physics & Astronomy

Senior Honours Project

Finding the first quiescent galaxies with the James Webb Space Telescope

Evan Jones
1st April 2022

Abstract

In this work, several analyses of high redshift quiescent galaxies in the COSMOS field are made. LePhare fitting results from the COSMOS2020 THE FARMER catalogue are used to find 24 high redshift quiescent galaxy candidates, which are then fit using BAGPIPES. A catalogue of $\sim 40,000$ of the brightest objects with the deepest imaging is created, to 20σ depth in the K_s-band. Mock photometry is generated for a population of quiescent galaxies in COSMOS and JWST NIRCam filters to compare the number of galaxies that could be detected.

5 out of 24 candidates can be reliably fit, with multiple objects not having reliable detections or suffering from confusion. Three galaxies are determined to be quiescent, but at low ($z \sim 3$) redshifts. One galaxy is at redshift $z = 4.7^{+0.1}_{-0.1}$, but is star forming. In the catalogue, six galaxies are identified with $4 < z < 6$ and no secondary solutions, one of which is quiescent. The photometric redshift is $z = 4.14^{+0.05}_{-0.06}$, with sSFR $= -10.29^{+0.10}_{-0.06}$ yr^{-1}. The LePhare and EAZY fitting included in COSMOS2020 broadly agree. For the mock photometry, the COSMOS detection rate is 52%, while JWST recovers up to 76% of quiescent galaxies.

Future work building on these results is discussed.

Declaration

I declare that this project and report is my own work.

Signature: Evan Jones Date: 01/04/2022

Supervisor: Dr. A. C. Carnall 10 Weeks

Contents

1 Introduction

Quiescent (or passive) galaxies are galaxies that have stopped forming stars, or *quenched*. They are of great interest as they make up the majority of massive galaxies in the local universe, and the quenching process is therefore an important aspect of galaxy evolution.

This introduction aims provide some motivation for studying quiescent galaxies, before discussing the difficulties in observing and identifying them. Then, some parameters of interest and how they are constrained are introduced. At the end, the project itself is introduced and outlined.

Despite the prominence of quiescent galaxies, there are open questions about the relative importance of potential quenching mechanisms (Schreiber et al. 2018), for example supernovae (Benson et al. 2003) versus AGN feedback (Cattaneo et al. 2009), and computational models currently poorly recreate the number density of quiescent galaxies. Cecchi et al. (2019) find simulations underestimate the number of massive, high redshift quiescent galaxies, while Davé et al. (2017) overestimate the number of local low mass quenched galaxies. Models keep improving, but as they do more precise measurements of a wider range of parameters are needed to constrain them.

Observationally there are two different quenching methods, *fast* and *slow* (Belli et al. 2019; Carnall et al. 2018; Wu et al. 2018). How physical quenching mechanisms relate to these observed ones is not yet well understood. Fast quenching is more important at higher redshifts, with the associated post-starburst objects being distinct from slowly quenched objects in mass, morphology, environment, and size (Belli et al. 2019). The fact they are generally elliptical galaxies residing in overdensities implies mergers play an important role in fast quenching (as discussed in Brodwin et al. 2013; Wu et al. 2014).

Slow quenching happens along the same timescales as a process called *gas starvation* or *strangulation* (Carnall et al. 2018), where galaxies run out of cold gas to form stars from. Peng et al. (2015) present strong evidence that local quiescent galaxies (smaller than $10^{11}\mathrm{M}_{\odot}$) quenched in the same way. From this it would appear that gas starvation is the physical mechanism behind slow quenching. However, there are many different ways this can come about; virial shock (Kereš et al. 2005) and AGN feedback (Cattaneo et al. 2009, mentioned above) are two popular examples.

Studying quiescent galaxies is difficult for a number of reasons. Brighter, higher mass stars evolve faster than lower mass stars. As a result, these high mass stars 'die' faster, leaving a population of lower mass stars that evolve more slowly. This means that the ages are more difficult to constrain for older, and hence quiescent, populations. A confounding factor is that a burst of star formation can outshine

the older population. Secondly, as new stars stop forming in a galaxy, the brighter, bluer star population decreases, so the galaxy gets fainter and redder. This makes them harder to observe.

Identifying galaxies as either passive or star-forming is made difficult by the fact that the bimodality of colour, mass, age, morphology, and environment in the local universe stops holding so strongly at higher redshifts (Schreiber et al. 2018). For example, a red galaxy with low redshift is most likely a massive quenched elliptical galaxy, but at higher redshifts the chance that it is a dusty star forming galaxy increases. Popular methods discriminate between quiescent and dusty galaxies by using multiple colours, like rest-frame UVJ or $NUVrJ$ colours (Girelli et al. 2019; Ilbert et al. 2013; Williams et al. 2009). Others use the specific Star Formation Rate (sSFR, defined as the ratio between star formation rate and stellar mass) (Carnall et al. 2020; Fontana et al. 2009; Merlin et al. 2018). Colour cuts, like UVJ, have been shown to strongly agree with sSFR selection (Carnall et al. 2019a; Leja et al. 2019), but as rest-frame colours and sSFRs are usually derived from the same model spectrum they are susceptible to the same errors.

There are several quantities that are useful in building models of the formation and growth of individual galaxies and the population as a whole: number density, stellar mass, age, metallicity, and Star Formation Histories (SFHs). To get the complete picture of formation and quenching, these need to be measured across cosmic time.

With spectra, parameters can be more strongly constrained than with Spectral Energy Distributions (SEDs) because characteristic breaks and absorption and emission lines are observed, or absent. This also means spectra are less susceptible to the age-metallicity-degeneracy. However, it is harder to get a high signal-to-noise (SNR) for spectra than it is for photometry, especially with fainter redder objects. Additionally, the features used in spectra are redshifted into the near-IR for $z \gtrsim 1$, making them much harder to observe because of the atmosphere and limitations of current instrumentation. Photometric surveys cover wider areas and can contain more objects than spectroscopic ones, so it is possible to survey large volumes of the universe, which is necessary for building and testing models.

When fitting models to SEDs with a Bayesian approach, as this paper will do, there are advantages and disadvantages. Having full posterior distributions for parameters allows degenerate solutions to be identified, so contaminants in quiescent galaxy samples (like dusty star forming galaxies) can be avoided. However, assumptions and priors have a big impact on the results. For example, the form of the SFH used (Carnall et al. 2019b).

The next generation of instruments, like the *James Webb Space Telescope* (JWST) and the *Extremely Large Telescope* (ELT) will gather high-SNR spectra and deeper observations, allowing stronger constraints and finding more galaxies

respectively. This is necessary, as while samples of quiescent galaxies at high ($\gtrsim 4$) redshifts are getting larger, they are still not statistically significant (Marsan et al. 2022). They will also be able to perform large photometric surveys of popular legacy fields, discovering new galaxies too red and faint for current optical telescopes (i.e. HST), and breaking through the confusion limit of Spitzer/IRAC observations. One example is the PRIMER (Public Release IMaging for Extragalactic Research) survey with JWST observing the UDS (Ultra-Deep South, Galametz et al. 2013) and COSMOS (Cosmic Evolution Survey, Scoville et al. 2007) fields. The combination of new and existing photometry will cover a wide range of wavelengths, and will increase the accuracy of spectra fit to SEDs from these fields (Bisigello et al. 2016).

This project has several science goals, all related to high redshift quiescent galaxies. First, the sample of 13 quiescent galaxies with redshifts $4.5 < z < 6$ identified in the COSMOS2020 THE FARMER catalogue by Weaver et al. (2022) is recreated, then re-fit using BAGPIPES (Bayesian Analysis of Galaxies for Physical Inference and Parameter EStimation) (Carnall et al. 2018) to confirm or dispute their results. Secondly, a sub-sample of sources from the COSMOS2020 THE FARMER catalogue are fit with BAGPIPES to create an independent catalogue of some of the brightest objects. This catalogue is then analysed to find high-redshift quiescent galaxies. Finally, the ability of JWST to detect quiescent galaxies over a range of masses and redshifts in the COSMOS field from the upcoming PRIMER survey is analysed.

In Section 2 the COSMOS2020 data is introduced, and 24 potential high redshift quiescent galaxies identified. How they are fit using BAGPIPES is described, before the results are presented. In Section 3 a catalogue of $\sim 40,000$ galaxies is created from a subset of the brightest (K_s-band) objects in the COSMOS field, finding 6 high redshift galaxies, one of which is quiescent. Section 4 analyses the abilities of the JWST to detect high redshift quiescent galaxies in the PRIMER survey. Finally, Section 5 discusses further steps to be taken, or that would have been taken if time permitted, followed by the conclusion in Section 6.

All magnitudes are quoted in the AB system: $m_{\mathrm{AB}} = 23.9 - 2.5\log_{10}(f_\lambda/\mu\mathrm{Jy})$. Calculations assume a Λ-CDM cosmology with $H_0 = 70\,\mathrm{km\,s^{-1}\,Mpc^{-1}}$, $\Omega_\Lambda = 0.7$, and $\Omega_M = 0.3$. A Kroupa (2001) initial mass function is assumed. Values provided are medians of posterior distributions, and errors are calculated from the 16th and 84th percentiles (1σ of a Gaussian distribution).

2 Quiescent Galaxies in the COSMOS2020 Survey

This section introduces the COSMOS2020 catalogue, and the 13 high redshift ($4.5 < z < 6$) quiescent galaxies reported by Weaver et al. (2022). The attempted

recreation of this sample is detailed, before the use of BAGPIPES to fit the galaxies is explained, and discussion of the results.

2.1 The Data

The COSMOS2020 survey (Weaver et al. 2022) is made up of observations covering the 2 $\deg^2$ COSMOS field, taken in bands ranging from 3000–80000 Å, from several ground- and space-based observatories. COSMOS2020 is different to previous releases, as the photometry was generated in two ways, using SEXTRACTOR (Bertin and Arnouts 1996), and a new code called THE FARMER (Weaver et al., in preperation).

The quiescent galaxies of interest were identified in the THE FARMER catalogue, and in this report the COSMOS2020 catalogue is taken to mean the catalogue made with THE FARMER photometry. There are $\sim 966,000$ sources detected, and the catalogue includes parameters (e.g. photometric redshifts, stellar mass) from the fitting codes LEPHARE (Arnouts et al. 1999; Ilbert et al. 2006) and EAZY (Brammer et al. 2008).

The survey is well suited to studying high redshift quiescent galaxies as it includes Ultra-deep UVISTA (McCracken et al. 2012) K_s-band measurements, reaching a 3σ depth of 25.2 magnitudes. Deep measurements in the K_s-band are important for detecting and constraining high redshift quiescent galaxies, as for redshifts between 4 and 6 the Balmer break is redshifted into the wavelength range of this filter.

For further details of the catalogue, including a full list of filters and telescopes involved, see Weaver et al. (2022).

2.2 Quiescent Sample Selection

Weaver et al. (2022) identify 13 potentially quiescent galaxies at redshifts $4.5 < z < 6.0$ in the COSMOS2020 survey, using photometric redshifts and rest-frame $NUVrJ$ colours determined by LEPHARE. These objects can be seen in the colour-colour plot in Figure 1a. The selection process they outline consists of the following steps.

Firstly, galaxies are binned by redshift. Secondly, the quiescent galaxies are identified using $NUVrJ$ colour selection, as described in Ilbert et al. (2013). In this scheme, quiescent galaxies are said to have $NUV - r > 3(r - J) + 1$ and $NUV - r > 3.1$. This a popular alternative to the UVJ cuts of Williams et al. (2009), with claims it is better at determining changes in SFR, and that it is better at separating quiescent populations from dusty contaminants (Arnouts et al. 2007; Ilbert et al. 2013).

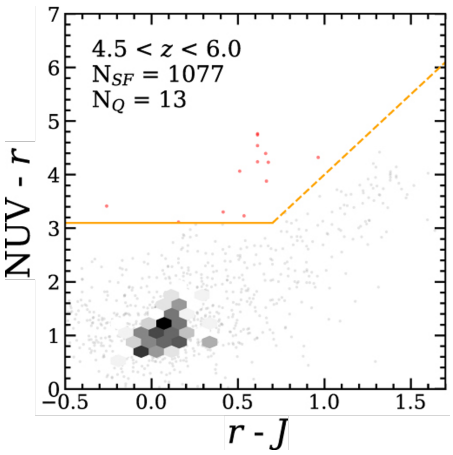

(a) COSMOS2020 high redshift colour-colour plot, adapted from Weaver et al. (2022).

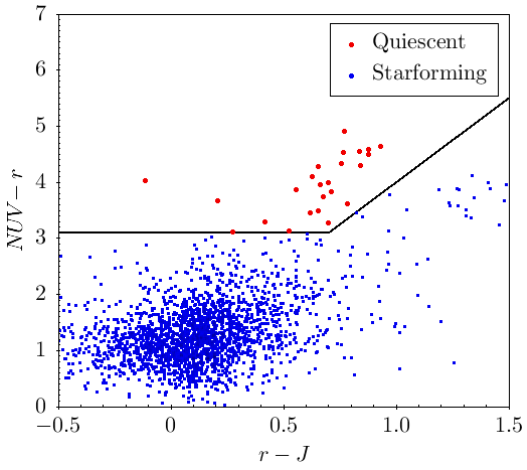

(b) Colour-colour plot for the recreated sample. Quiescent galaxies are above the solid black lines, marked in red.

Figure 1: Comparison of the two samples. On the right, 24 quiescent galaxies have been identified using rest-frame $NUVrJ$ colours. Unfortunately the 13 galaxy sample from Weaver et al. (2022) could not be recreated so the exact galaxies could not be tested with BAGPIPES. However, the sample created here has some overlap. The orange and black demarcations are the $NUVrJ$ selection box.

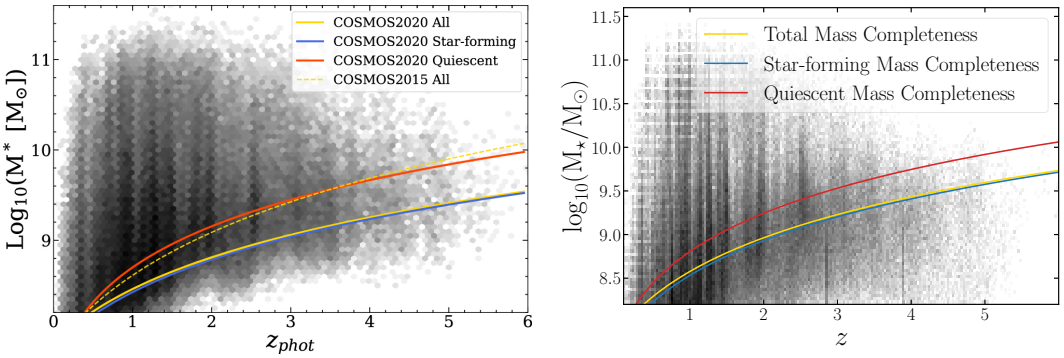

(a) COSMOS2020 mass completeness limit, adapted from Weaver et al. (2022).

(b) Derived mass completeness limit.

Figure 2: Comparison of the mass completeness limits, over 2D histograms of the survey. The mass completeness for the quiescent population was not included in Weaver et al. (2022), so needed to be re-derived. For the redshift range of interest they agree.

The sample is then analysed for mass completeness following the method outlined in Pozzetti et al. (2010). This consists of taking the magnitude limit of a survey, $m_{\rm lim}$, scaling the i-th mass by a factor of $10^{0.4(m_i - m_{\rm lim})}$, and setting the 95th percentile of this distribution to find the limit. This was repeated separately for the star forming and quiescent samples in bins of redshift. The mass completeness limit for the quiescent population was not provided, so had to be re-derived as $\log_{10}(M_\star/M_\odot) > -2.11 \times 10^8(1+z) + 2.65 \times 10^8(1+z)^2$. The comparison between the original and the limit computed is shown in Figure 2. From the figure, it is clear they are close for high redshifts. For low redshifts they are not expected to be close as Weaver et al. (2022) use a different, K_s-band based, method.

In summary, the criteria for the 13 quiescent galaxies are:

- $4.5 \leq z_{\rm LePhare} \leq 6$
- $NUV - r > 3(r - J) + 1$
- $NUV - r > 3.1$
- $\log_{10}(M_\star/M_\odot) > -2.11 \times 10^8(1+z) + 2.65 \times 10^8(1+z)^2$

Applying the constraints above yields a sample of 572 objects, much larger than the 13 expected, so additional constraints are included: the galaxies must have deep imaging and be outside masked regions (not close to bright objects); LePhare should find no secondary solution; and the galaxy has to be brighter

than 26th magnitude in IRAC Channel 1 (the 3σ depth of this survey). This creates a sample of 24 quiescent galaxies, shown in Figure 1b. The two samples are different, but contain some overlap. For a comparison, see Figure 1.

The full list of criteria to create this sample, alongside those listed above, are:

- FLAG_COMBINED = 0 (deep imaging and outside bright sources)
- lp_zp_2 = NULL (no secondary solution found)
- IRAC Channel 1 < 26

2.3 Fitting with BAGPIPES

The sample is fit using BAGPIPES (Carnall et al. 2018), a code that fits galaxy spectra to photometry using Bayesian inference. The Bayesian method is useful because it generates full posterior distributions, which can be used to derive errors and check for secondary solutions. Checking for secondary solutions is important because of the numerous factors that can redden a galaxy, so the ability to see if photometry can be described by a low redshift, dusty solution as well as a high redshift one is important in determining the nature of objects.

Fourteen bands are used in fitting: u^*, g, r, i, z, y, Y, J, H, K_s, and IRAC Channels 1, 2, 3, and 4. The signal-to-noise ratio (SNR) is capped at 10 for IRAC channels 1 and 2, 5 for channels 3 and 4, and 20 for all other bands (corresponding to uncertainties of 5%, 10%, 20%). This is to account for systematic errors dominating over Poisson errors at high SNRs (e.g. Carnall et al. 2020; Weaver et al. 2022). Narrow bands typically have large errors, so have poor constraining power, and therefore are not used in fitting, despite their inclusion in the COSMOS2020 catalogue.

2.3.1 Priors

The priors used are based on Carnall et al. (2020). The star formation history (SFH) is parameterised as a double power law, described in Carnall et al. (2018):

$$\mathrm{SFR}(t) \propto \left[\left(\frac{t}{\tau} \right)^{\alpha} + \left(\frac{t}{\tau} \right)^{-\beta} \right]^{-1}. \tag{1}$$

This parameterisation has been shown to describe observed and simulated data well (Behroozi et al. 2013; Carnall et al. 2019b). The turnover time, τ, is allowed to vary uniformly between 0.1 Gyr and the age of the universe at the redshift z, $t_{\mathrm{age}}(z)$. The falling (α) and rising (β) slopes are allowed to vary as $-2 \leq \log_{10}(\alpha) \leq 3$ and $-2 \leq \log_{10}(\beta) \leq 3$.

Parameters		Range
z,	Redshift	Uniform from 0 to 10
$M_\star/M_\odot$,	Stellar Mass formed	Logarithmic from 1 to 10^{13}
$Z/Z_\odot$	Stellar Metallicity	Logarithmic from 0.1 to 2.5
α	Double power-law falling slope	Logarithmic from 10^{-2} to 10^3
β	Double power-law rising slope	Logarithmic from 10^{-2} to 10^3
τ/Gyr	Double power-law turnover time	Uniform from 0.1 to $t_{\text{age}}(z)$
A_V/mag	Total V-band attenuation	Uniform from 0 to 4

Table 1: Priors for fitting. Uses the Calzetti et al. (2000) dust attenuation law. 'Logarithmic' means the priors are uniform in $\log_{10}$ space. $t_{\text{age}}(z)$ is the age of the universe at the redshift of the galaxy.

The magnitude of dust extinction, A_V, was initially set to range from 0–8, but this returned unphysical solutions, with $A_V \gtrsim 7$, so is reduced to $0 \leq A_V \leq 4$. The objects were also originally fit with a Salim et al. (2018) dust attenuation law. When fitting with a Salim et al. (2018) or Calzetti et al. (2000) law the results are the same, but when using a Calzetti et al. (2000) law the fitting is more consistent with the catalogue in Section 3, so it is used instead. This could potentially create less accurate fits, but no major differences in the posterior distributions are observed.

The stellar mass, $M_\star$, is allowed to vary as $0 \leq \log_{10}(M_\star/M_\odot) \leq 13$, and metallicity as $-1 \leq \log_{10}(Z/Z_\odot) \leq 0.4$, where $M_\odot$ and $Z_\odot$ are the mass and metallicity of the Sun, respectively. $Z_\odot$ is taken to be 0.02. The redshift, z, is allowed to vary uniformly between 0 and 10. For a summary of these priors, see Table 1.

2.4 Results and Discussion

As a result of fitting, only one third of galaxies are found to lie in the original redshift range $4.5 < z < 6$. On top of this, only 5 out of 24 galaxies have a χ^2 value that implies a good fit, and only one of these has a redshift greater than 4.5. Spectra and cutouts for the five well fitted objects are shown in Figures 3 and 4. Spectra and cutouts for all objects are shown in Appendix A.

A good fit is defined in this paper to mean having a χ^2 value that corresponds to 3σ confidence for a Gaussian distribution. For 14 bands of data and seven fitted parameters, there are 6 degrees of freedom, so the maximum χ^2 is 21.74.

Cutting the catalogue using IRAC channel 1 potentially caused issues because the lower angular resolution means objects are more likely to be confused. Other surveys, for example Muzzin et al. (2013), use the K_s-band.

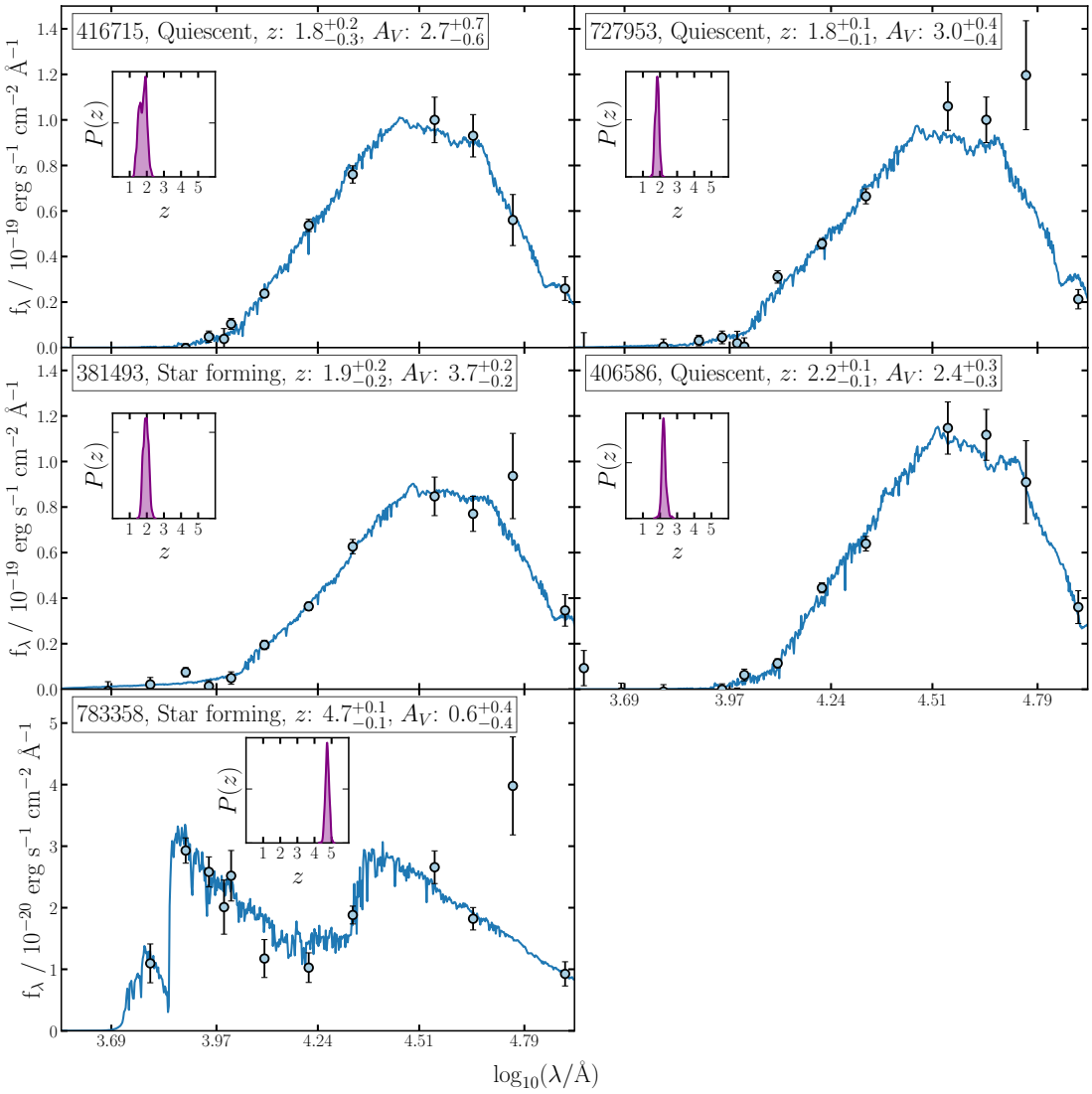

Figure 3: The five objects with a low enough χ^2. To have objects so dusty yet passive is very unusual.

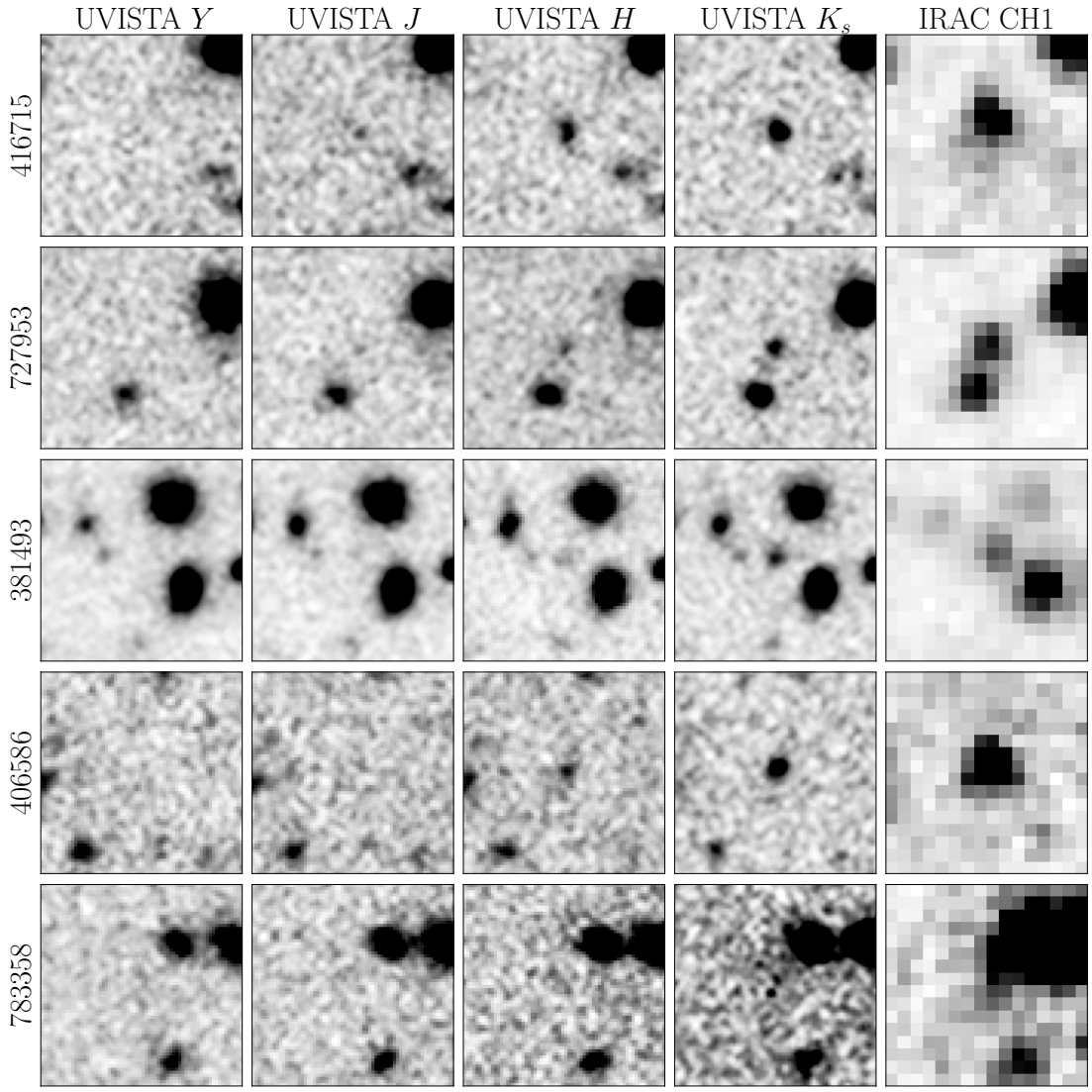

Figure 4: Cutouts, 10×10 arcseconds, of the five objects with a low enough χ^2. To have objects so dusty yet passive is very unusual. There are primarily clear detections in the K_s-band, and nothing bluewards of this, as expected from the $NUVrJ$ selection. Only the final object shows possible confusion.

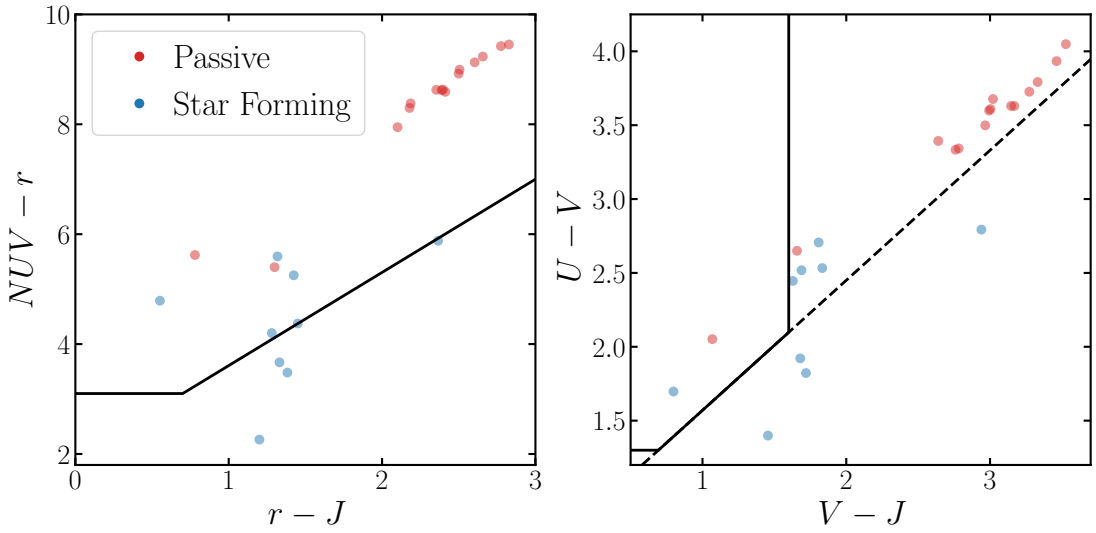

Figure 5: Comparing rest-frame $NUVrJ$ and UVJ colours of the 24 objects, generated from our fitted spectra. The points are coloured based on their sSFR; red points have a low enough sSFR to be considered passive, blue points do not. On each diagram the black demarcations mark the selection boxes, mentioned in text. The dotted black line in the UVJ diagram is an extension of the diagonal UVJ cut.

Figure 5 shows rest-frame $NUVrJ$ and UVJ colours, generated by BAGPIPES. The selection criteria from Weaver et al. (2022) and Williams et al. (2009) are marked with solid black lines. To identify quiescence, the specific star-formation rate (sSFR) criterion $\text{sSFR} < 0.2/t_{\text{age}}(z)$ is used instead, to compare the different colour-colour methods. This selection criterion has been used in several recent studies (e.g. Carnall et al. 2020; Pacifici et al. 2016), and corresponds to the SFR falling below 10% of its mean value. This is different to the initial sample selection, in Figure 1, where colour was used. In Figure 5 galaxies are colour-coded based on their sSFR, with red points representing quenched galaxies, and blue points representing galaxies with ongoing star formation.

It can be seen that generally the galaxies occupy the same space on both planes (albeit with some scaling). The difference is the regions where the sSFR and colour-colour selection agree. There is a lot of agreement between sSFR and $NUVrJ$ colour, with all the quiescent objects selected for by both. There is a small amount of contamination too, with four sSFR-passive objects in the quiescent selection box. The results are very similar when considering the diagonal UVJ criterion, $U-V > 0.88(V-J)+0.69$. However, when the vertical cut ($V-J < 1.6$) is introduced, some contaminants are removed, but a larger number of dusty sSFR-

passive galaxies are removed too.

Unfortuntely, it is unclear to what extent the detection and fits of these objects are accurate. This makes drawing conclusions difficult. When looking at the imaging, it would appear many objects have unclear detections, and/or suffer from confusion in the IRAC channels. The χ^2 values of many of the models imply poor fits to the data. The agreement with the original fits is also poor; as mentioned above only one third of the new fits are in the correct redshift range, and only one of these is well-fitted.

When considering the well-fitted objects, objects 416715, 727953, and 406586 are all quiescent by sSFR, but incredibly dusty compared to standard levels in quiescent galaxies ($A_V \sim 3$ vs. ~ 0.5). They are also lower redshift than the initial selection, with $z \sim 2$. However, there are no higher redshift solutions in the posteriors. Generally colour cuts remove dusty galaxies, but some studies (e.g. Schreiber et al. 2018) do report young, dusty quiescent galaxies.

If the derived parameters are accurate then this would show that the rest-frame UVJ colour selection of Williams et al. (2009) excludes dusty quiescent objects, which would certainly be of interest to study. It demonstrates that modified UVJ selection or $NUVrJ$ selection is necessary for building samples. However, if the results are not accurate then it implies the opposite; $NUVrJ$ permits too many contaminants into samples so should be avoided. Further investigation into these objects, for example spectra or radio measurements that probe star-formation obscured by dust that can determine the SFR accurately, should be carried out.

3 Fitting a New Catalogue

In this section the creation of a catalogue consisting of the brightest objects in the COSMOS field is discussed, starting with choosing the subset of objects to fit. Following this is the discussion of the fitting, then analysis of the sample and identification of potential high-redshift quiescent galaxies. Following this is a comparison of this to other studies.

3.1 Catalogue Creation

Due to the short length of this project it would not have been possible to fit all $\sim 966,000$ objects in the COSMOS2020 catalogue. Instead, a subsample was generated, by making several cuts. Firstly, the sample was cut in the K_s-band. The K_s-band is ideal for finding quiescent galaxies at redshifts 4–6 because the Balmer break is redshifted into this band for these redshifts. The sample was initially cut at the 5σ detection limit, but after running for several weeks it was decided instead to cut at 20σ, as this was close to the number of objects fit, and was more

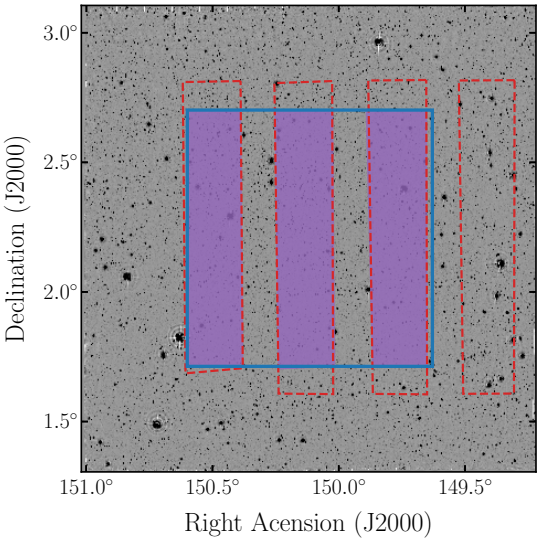

Figure 6: A diagram showing the area of the original cosmos field this catalogue covers. The dashed red lines are the UVISTA ultra-deep stripes, the blue box is the central square degree. The purple regions where they overlap is the area covered by this catalogue. The background region is the CFHT u^* mosiac (McCracken et al. 2010)

reasonable for the timescale involved. In order to get well fitted SEDs only objects with valid photometry in all 14 bands listed in Section 2.3 were included. In order to get the deepest possible measurements, only objects in the UltraVISTA Ultra-deep stripes and the central $\sim 1\,\mathrm{deg}^2$ of the COSMOS field, where the ancillary photometry is deepest, were included. As in Section 2, the galaxies must also not be flagged as close to a bright source. The final sample consists of $41,479$ objects. Figure 6 shows the regions of the COSMOS field included.

In summary, the cuts are:

- $K_s < 23.14$
- Photometry exists for all 14 bands
- $149.629 <$ Right Ascension < 150.600
- $1.713 <$ Declination < 2.702
- FLAG_UDEEP $= 0$ (Inside UVISTA Ultra-deep stripes)
- FLAG_COMBINED $= 0$ (Not near bright sources)

These 41,479 objects were then fit with BAGPIPES, using the same priors as above, listed in Table 1. The distinction is that the probabilities were sampled over a finer grid (1,000 points instead of 400). This increases accuracy at the expense of computing time. To fit such a large number of objects, cuillin[1], the Institute for Astronomy's computing cluster, was used.

3.2 Results

After all objects were fit the catalogue was cut by χ^2 to select well-fit galaxies. Again, only fits with $\chi^2 < 21.74$ were kept, corresponding to 3σ confidence for a Gaussian distribution. This reduces the catalogue to 18,650 objects. Of these 18,650 objects, 4659 (25%) are passive when cutting by sSFR, and 4794 (26%) when using the $z = 0$ UVJ selection from Williams et al. (2009). The sSFR criterion is $\mathrm{sSFR} < 0.2/t_{\mathrm{age}}(z)$. Figure 7 shows the UVJ colours of the galaxies in the catalogue. The black lines separate the passive galaxies from the star forming population. The points are coloured based on if they are passive according to the sSFR selection, with red markers for galaxies that are passive, and blue for star forming. It is clear that the two methods are generally in very good agreement. At high redshifts the agreement is poorer, as more high redshift passive galaxies are below the horizontal cut. The evolution of high redshift passive galaxies towards the bottom left of the box is discussed by Carnall et al. (2020), and Merlin et al. (2018) demonstrate that the horizontal cut selects against rapidly quenched galaxies, which dominate at high redshifts.

In the sample, six high redshift ($4 < z \leq 6$) galaxies have been identified, and their spectra are shown in Figure 8, alongside their COSMOS2020 IDs, redshift posterior distributions, their dust levels, and if they are star forming or passive. In the case of all these galaxies, the sSFR and UVJ selections agree. From the posterior distributions it can be seen there are no secondary, low redshift solutions.

Figure 9 shows cutouts, 10 arcseconds to a side, of the objects in several bands. All of the bands show convincing detections. Most of the objects are extended and well separated, but objects 436956 and 791411 appear to suffer from confusion in the IRAC imaging.

Specifically of interest is object 188115, which is flagged as quiescent by both UVJ colour and sSFR. Its fitted spectrum, alongside posterior distributions of several quantities of interest, are shown in Figure 10. When looking at the imaging the galaxy becomes considerably less visible in wavelengths bluer than the UVISTA H-band, consistent with a Balmer break at a redshift ~ 4. The galaxy is a massive, high redshift, quiescent galaxy, with $M_\star = 11.35^{+0.04}_{-0.05}\ M_\odot$, $z = 4.14^{+0.05}_{-0.06}$, and $\mathrm{sSFR} = -10.29^{+0.10}_{-0.06}\,\mathrm{yr}^{-1}$, over 4σ below the limit of $-9.86\,\mathrm{yr}^{-1}$. The shape of the

[1] http://cuillin.roe.ac.uk/

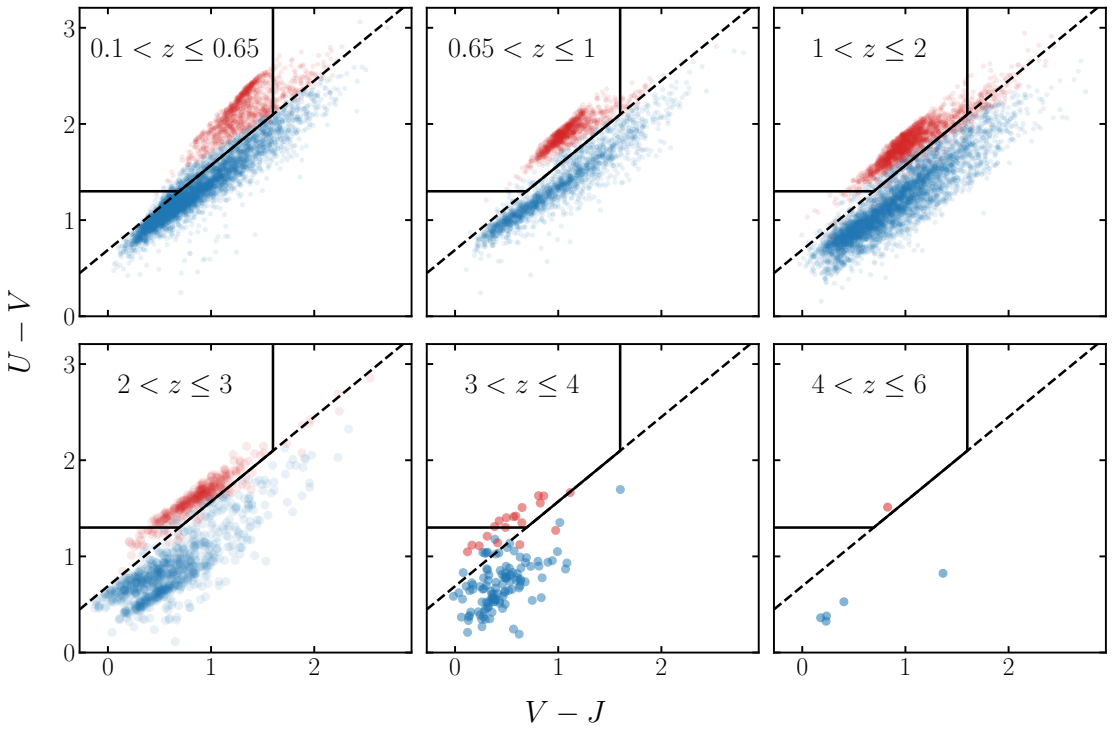

Figure 7: Rest-frame UVJ colours for well-fit galaxies, binned by redshift. The median errors are 0.06 in $V-J$ and 0.04 in $U-V$. The solid black demarcations are the $z = 0$ UVJ selection criteria of Williams et al. (2009). The dashed black line is an extension of the diagonal solid line. sSFR and the diagonal UVJ selections agree well, but the horizontal cut not as much. It seems likely that these are post-starburst galaxies, which are known to occupy this region of the plot (Wild et al. 2014), but this was not analysed

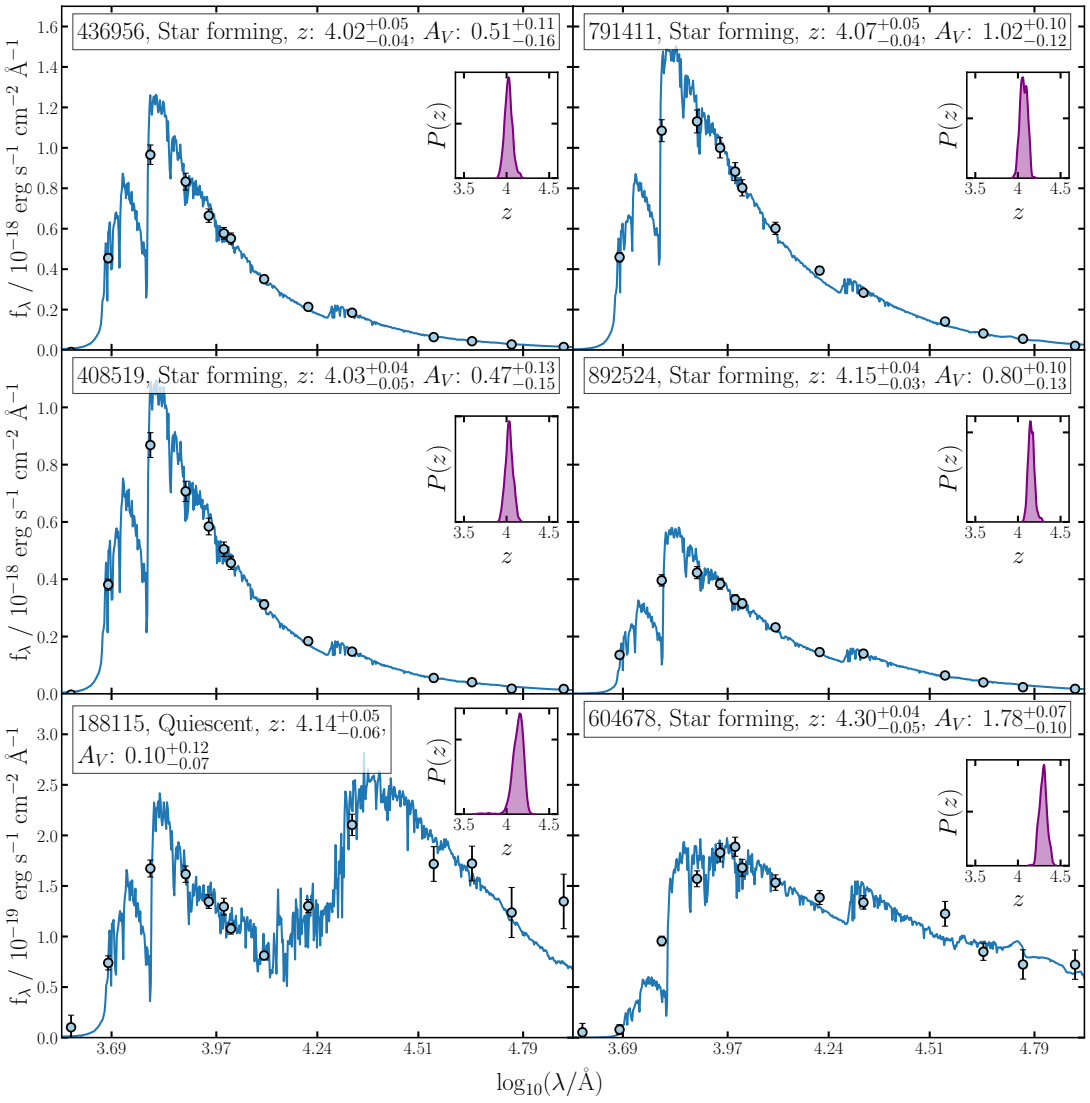

Figure 8: The six high redshift galaxies in the bottom right pane of the UVJ plot in Figure 7. Each plot shows the observed data, the median of the spectrum posterior, the ID, whether the galaxy was flagged as quiescent or not, the redshift posterior and the redshift and dust extinction values. None of these have secondary low redshift solutions.

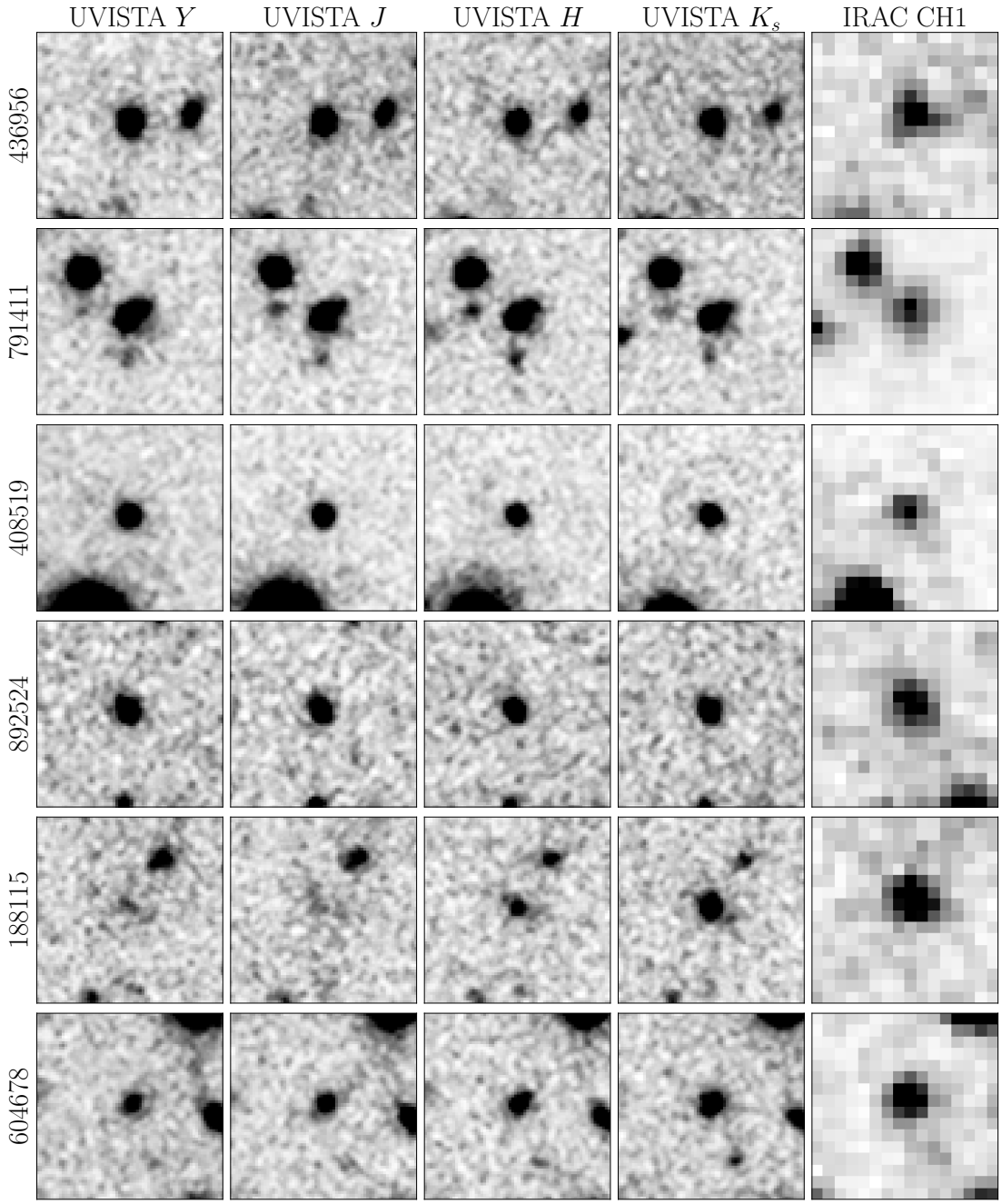

Figure 9: 10×10 arcsecond cutouts, centred on the six high redshift galaxies, in UVISTA Y, J, H, K_s bands and IRAC Channel 1. This shows that the objects are typically extended, well seperated, with strong detections in all bands, with the exception of the quiescent galaxy 188115, which drops in magnitude blue-wards of the H band.

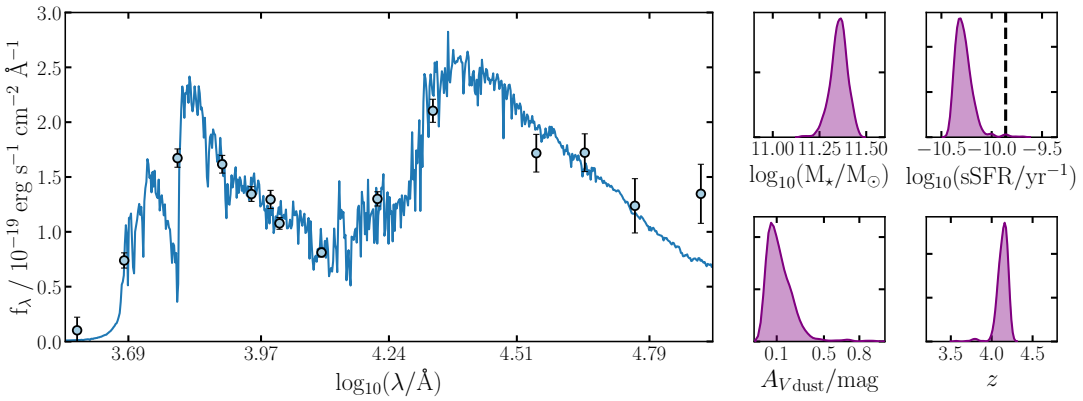

Figure 10: Fit for object 188115. The four panels on the right show posterior distributions for redshift, dust, stellar mass, and specific star formation rate. The dashed black line shows the limit to be considered quiescent by sSFR. It was selected as it is quiescent by UVJ cuts too.

spectrum still shows a relatively high amount of blue flux, which could imply the galaxy has only recently quenched, as the young bluer stars have not yet evolved off the stellar main sequence. The quenching timescale is $\sim 0.6\,\text{Gyr}$, consistent with a post-starburst galaxy and fast quenching, thought to be dominant at high redshifts (Belli et al. 2019).

Several quiescent galaxies have been spectroscopically confirmed at similar ($z \sim$ 3–4) redshifts (Forrest et al. 2020; Schreiber et al. 2018; Valentino et al. 2020), so it is reasonable to assume that the fitting has been successful. However, it is still useful to compare results. The fitting carried out with LePhare and eazy in Weaver et al. (2022) broadly agree, but find lower redshifts and higher star formation rates. Figure 11 compares these values and errors. The VIMOS Ultra-Deep Survey (Le Fèvre et al. 2014), zCOSMOS (Lilly et al. 2007), and ZFOURGE (Straatman et al. 2016) catalogues were searched for the object, but it could not be found. Finding photometric redshifts would help determine the accuracy, but spectroscopic redshifts are typically much more accurate so would confirm this object's status.

A useful way to compare the accuracy of fitting is to find overlap between other surveys. The object found by Valentino et al. (2020) to have a spectroscopically confirmed redshift ~ 3.77 is object 634562 in the COSMOS2020 catalogue (466654 in COSMOS2015), but is not included in this project's catalogue as it outwith the central square degree. Three objects from Schreiber et al. (2018), ZF-COS-20032, ZF-COS-20133, and ZF-COS-10559, were found in the initial 5σ limited selection, but were not bright enough to be fit in the final 20σ catalogue. The first two

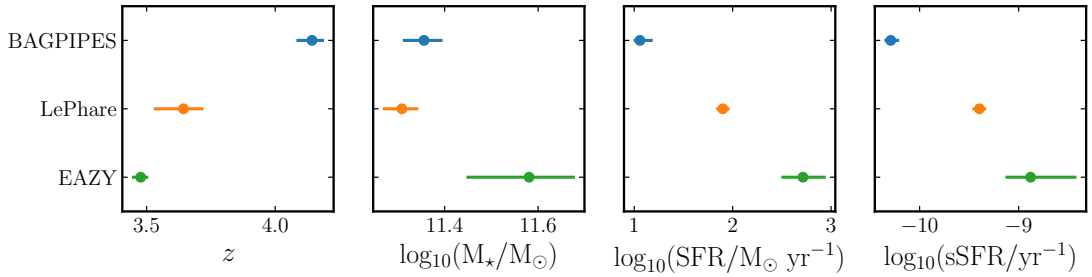

Figure 11: Comparing redshift, stellar mass, star formation rate and specific star formation rate for object 188115.

objects would have been especially useful comparisons to make as they also had spectroscopic redshifts. Marsan et al. (2022) create a catalogue over a similar area of the COSMOS field, but have not released it. This would have been a very useful tool for comparison.

4 Detection Power of the JWST

PRIMER (Public Release IMaging for Extragalactic Research, Dunlop et al. 2021) is an upcoming deep public observation run using the James Webb Space Telescope (JWST). It will use the NIRCam (Rieke et al. 2005) and MIRI (Rieke et al. 2015; Wright et al. 2015) instruments to measure the magnitudes of galaxies down to $m \sim 29$, over $\sim 400\,\mathrm{arcmin}^2$, with $\sim 144\,\mathrm{arcmin}^2$ in the COSMOS field. In this section, the ability of JWST to detect high redshift quiescent galaxies in this survey is quantified and compared to a similar analysis of COSMOS2020. For similar observing conditions (exposure time, background noise, etc.) the depths will be similar, so the analysis will hold. Apart from the depths, the analysis is perfectly general to any other observations.

4.1 Generating Photometry

BAGPIPES has the ability to generate spectra for model galaxies, drawing properties at random from a given distribution. To begin with, $1,000,000$ of these random galaxies were generated, using the same probability distrutions as the priors from Section 2.3 (see Table 1). The only differences are now the metallicity is fixed at solar metallicity ($Z = Z_\odot = 0.02$), and the lower limits for mass and redshift have been increased to $10^8 \mathrm{M}_\odot$ and 3 respectively. In summary: the rising and falling slopes are sampled logarithmically between 10^{-2} and 10^3; the turnover time is sampled uniformly from 0.1 Gyr to the age of the universe; the mass logarithmically

from 10^8 to 10^13 solar masses; the total V-band dust extinction uniformly from 0 to 4; and redshift uniformly from 3 to 10.

Of these, $\sim 160,000$ are physical (do not start forming before the beginning of the universe, quench after they form, etc.) and quiescent. The next step is to generate mock photometry in the eight NIRCam bands PRIMER is using: F090W, F115W, F150W, F200W, F277W, F356W, F410M, and F444W. This is again something BAGPIPES has the capabilities for. The code returns fluxes through each filter, which are converted to AB magnitudes.

After generating photometry in all NIRCam bands for the $\sim 160,000$ galaxies, galaxies are determined to be detected or not in each band. A galaxy is said to be detected in a band if the magnitude is less than or equal to the depth provided in the PRIMER proposal (private correspondence) for that band. The total number of galaxies detected in any band is calculated, before being binned by mass and redshift. This is used to calculate the percentage of galaxies detected in a bin, as galaxies are not generated uniformly in mass and redshift so total number detected is uninformative. The average number of bands a galaxy is detected in is also calculated for each bin. This is repeated for each of the three total integration times PRIMER will cover; 28 minutes, 42 minutes, and 1 hour 24 minutes. In this order, the depth increases, but the area covered decreases.

4.2 Results

The total percentage of galaxies recovered is very good for all integration times. The shallowest imaging is calculated to detect 71% of galaxies above a mass of $10^8 M_\odot$ and a redshift of 3. This increases to 76% for the deepest imaging. This is only considering NIRCam imaging, so it is possible these numbers will increase once the two MIRI bands are included. Figure 12 shows 2D histograms of the percentage of galaxies recovered by JWST, and the average number of bands the galaxy is detected in, as functions of mass, redshift, and exposure time.

It is possible to compare the PRIMER survey to COSMOS2020 by repeating the process outlined above, but generating photometry through the COSMOS filter subset used throughout this paper. This yields a detection rate of only 52%, worse than even the shallowest PRIMER imaging. A comparison of how detection rate changes as a function of redshift and stellar mass between COSMOS2020 and the deepest PRIMER imaging (1 hour 24 minute total integration) is shown in Figure 13.

It is worth discussing the continued need for other photometry, even with these new data. Only $\sim 10\%$ of the galaxies are detected in all eight bands, and these have the highest mass and lowest redshift. To fit accurate parameters to the spectral energy distributions over the full range of newly detected galaxies, deep measurements in many bands covering a wide range of wavelengths are necessary.

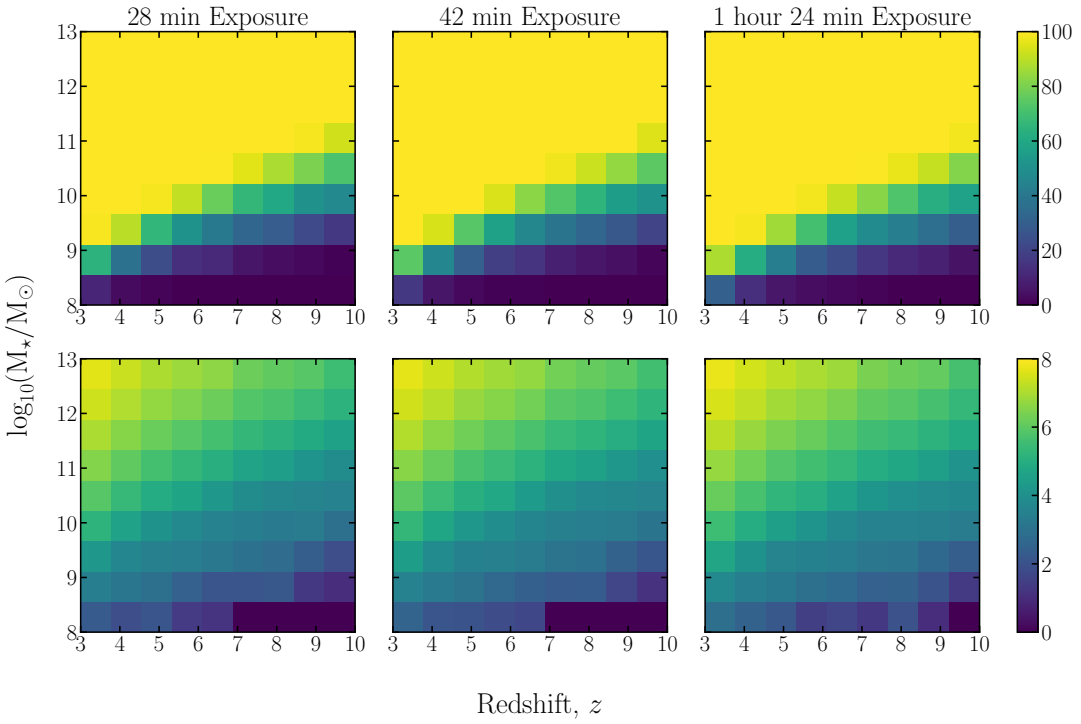

Figure 12: The top row shows the percentage of generated galaxies that were detected in at least one band. The bottom row shows the average number of bands an object in each bin was detected by. The columns show increasing depth, but decreasing area.

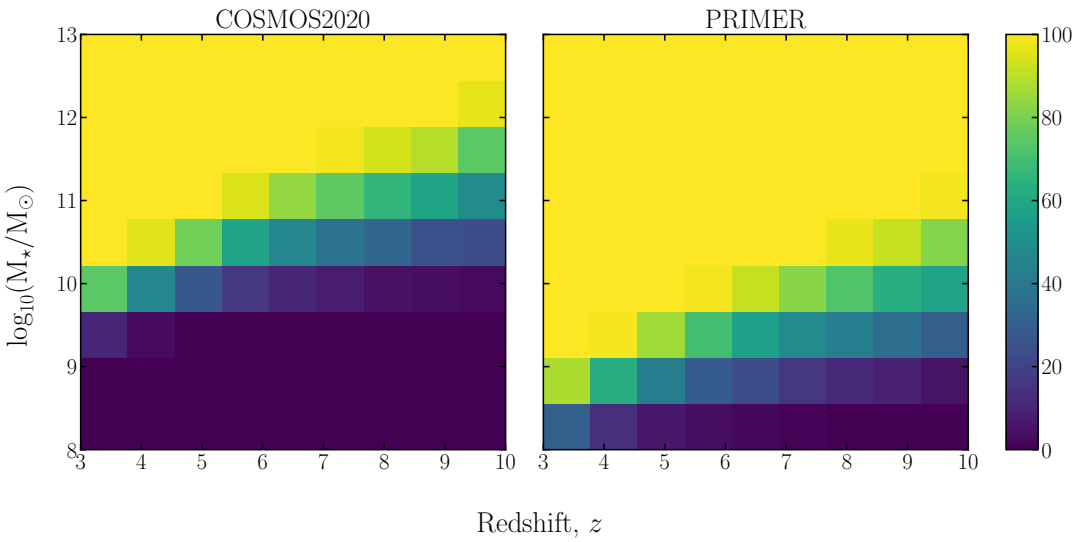

Figure 13: Detection rate for COSMOS2020 reported 5σ depth (Weaver et al. 2022) versus detection rate for PRIMER survey's 1 hour 24 minute exposures.

For example, Bisigello et al. (2016) show that adding optical bands is necessary to avoid dusty low redshift contaminants in high redshift samples, as the optical bands can constrain the Lyman break.

The next step, which there was not enough time to complete, would be to fit the generated photometry using BAGPIPES. This would show how well the galaxies' properties, such as redshift, could be constrained. However, due to the short duration of this project it was not possible to extend the analysis so deeply.

5 Further Steps

Due to the limited duration of this project (10 weeks), there are numerous ways that it could be improved or built upon with more time. This section will discuss improvements and next steps for the fitting of a new catalogue and its analysis (Section 3), then for the analysis of the JWST PRIMER survey (Section 4).

5.1 Catalogue Fitting

Similar studies include measuring the number density of quiescent galaxies to compare to other reports and simulations as a part of their results and discussion (e.g. Carnall et al. 2020; Schreiber et al. 2018). With more time, this would provide a useful comparison for results up to redshift 4, where there are enough galaxies to

get meaningful results. Spectroscopic follow ups for the high redshift objects, at least the galaxy identified as quiescent, would be a natural next step too. This would confirm redshifts, masses, sSFRs, and ages constrained with fitting. If this was not possible, comparisons between the photometric redshifts and any available spectroscopic redshifts for the entire catalogue could be compared to see how accurate the photometric results are (e.g. Weaver et al. 2022).

For fitting the new catalogue presented in this report (Section 3), numerous improvements could be made with more time or in future work. In the literature there are many other aspects taken into account when generating spectra (e.g. Carnall et al. 2019a, 2020) that BAGPIPES has the capability to simulate. For example, it would be beneficial to account for the fact young stars reside in dustier regions, so have more extreme attenuation than the general population. Another aspect is nebular emission, which was not included. Codes such as CLOUDY (Ferland et al. 2017) simulate the spectra as light passes through nebulae, including line and continuum emission. Other models of dust attenuation, like that of Salim et al. (2018), could also provide more accurate results. There was no difference in Section 2, but for a larger sample size it could find secondary solutions. Finally, the catalogue could be improved by the inclusion of dust radiation. When included in fitting the 24 COSMOS2020 objects there was no difference in posteriors, but in a larger sample it could be useful for finding dusty, low redshift solutions that contaminate UVJ selected samples. BAGPIPES calculates emission assuming energy balance using the models of Draine and Li (2007).

When analysing the fits, the objects with high χ^2 values tended to be over-constrained by the IRAC bands, namely channels 3 and 4. It could improve fitting to remove these bands. However, the IRAC observations are the only ones covering these wavelengths, which are important for high redshift galaxies. It would therefore be beneficial to run a similar catalogue fitting, with the suggestions above, using upcoming JWST data instead of or alongside Spitzer IRAC observations. This would improve the accuracy and constraining power of the fitting, and hence the accuracy of the catalogue.

With more time, it would be good to expand the sample size, by depth and area. This would facilitate easier comparison with other works, as it is more likely that objects, such as those already mentioned, would be included in the catalogue. Expanding the size of the catalogue also increases the chances of finding more interesting objects, like higher redshift quiescent galaxies. This is especially true when increasing depth, as these are often faint objects.

5.2 JWST

One of the most interesting ways the analysis of the JWST PRIMER survey could be improved is by fitting spectra to the mock photometry generated. By comparing

the true redshifts, masses, and star-formation histories to those constrained by SED fitting a detailed picture of the strengths and limitations of JWST can by built up. It is also possible to generate mock photometry for ancillary data (e.g. HST optical bands) to compare the raw ability of JWST to the ability of the JWST used in tandem with other telescopes (similar to Bisigello et al. 2016). The analysis of detections was also limited to three dimensions: time, redshift, and mass. This could be expanded by considering how additional factors, like dust, effect the detection rate.

The simulated observations can also be made more realistic. For example, Kauffmann et al. (2020) generate a population of galaxies, including contaminants such as galactic stars. They use this to create images, which they extract photometry from, before fitting the SEDs to compare the recovered and true parameters. However, this is beyond the scope of this project to consider in future studies.

6 Conclusion

In this work, the LePhare fits from the COSMOS2020 the farmer catalogue (Weaver et al. 2022) were used to find 24 high redshift quiescent galaxy candidates. bagpipes (Carnall et al. 2018), a Bayesian SED fitting code, was used to fit spectra to the SEDs. The model used allowed redshift to vary freely, used the Calzetti et al. (2000) dust attenuation law, and a double power law SFH parameterisation. Only five of the galaxies could be reliably fit, with a χ^2 corresponding to a 3σ Gaussian confidence interval. Looking at the imaging, multiple objects did not have reliable detections, or suffered from confusion. Three galaxies were determined to be quiescent, but at low ($z \sim 3$) redshifts. Only one galaxy was high redshift, with $z = 4.7^{+0.1}_{-0.1}$, but was star forming.

Next, a catalogue was created from a subsample of $\sim 40,000$ of the brightest objects in the COSMOS field, fitted using bagpipes and the same model as above. The catalogue reaches a 20σ depth in the K_s-band. Six galaxies were identified with $4 < z < 6$. One of which, 188115, is quiescent. The photometric redshift is $z = 4.14^{+0.05}_{-0.06}$, with $\mathrm{sSFR} = -10.29^{+0.10}_{-0.06}\,\mathrm{yr}^{-1}$, over 4σ below the limit of $0.2/t_{\mathrm{age}}(z)$. The parameters are all well constrained, with no secondary solutions. The object was sought after in other surveys (Le Fèvre et al. 2014; Lilly et al. 2007; Straatman et al. 2016) with the aim of comparing results, but it could not be found. Spectroscopic results in particular would have been useful for analysing quality of fit. The bagpipes fit was compared to the LePhare and eazy fitting included in COSMOS2020, which broadly agree.

High redshift quiescent galaxies have been found in the COSMOS field by Schreiber et al. (2018) and Valentino et al. (2020), but did not make it into this catalogue. This is because the catalogue only consists of bright objects in a small

region of the survey.

The final aspect of this project was generating mock photometry for a range of quiescent galaxies through JWST NIRCam filters, to determine how many galaxies would be detected as a function of mass and redshift in the PRIMER survey (Dunlop et al. 2021). This was repeated for the COSMOS bands used throughout this paper, and it was found that COSMOS detected 52% of quiescent galaxies, while JWST recovered 71% in its shallowest PRIMER observations, and 76% in the deepest.

Future steps would involve continuing to run the fitting code to build the catalogue down to fainter magnitudes, then covering a greater region of sky. This would enable more objects to be found. This allows for more comparison to other similar surveys, and a higher chance of finding more high redshift quiescent galaxies. Additionally, spectroscopic follow ups would be ideal for confirming if objects are truly high redshift and quiescent. A final improvement could be made by considering more advanced, but computationally expensive, models.

For the JWST PRIMER analysis, using BAGPIPES to fit spectra to the generated photometry would allow analysis of how well quiescent galaxies' properties can be constrained, as opposed to only considering if they can be detected, and in how many bands.

This paper made extensive use of the Matplotlib[2] (Hunter 2007) and Astropy[3] (Astropy Collaboration et al. 2013, 2018) libraries.

References

Arnouts, S. et al., "Measuring and modelling the redshift evolution of clustering: the Hubble Deep Field North", MNRAS **310**, 540 (1999).

Arnouts, S. et al., "The SWIRE-VVDS-CFHTLS surveys: stellar mass assembly over the last 10 Gyr. Evidence for a major build up of the red sequence between z = 2 and z = 1", A&A **476**, 137 (2007).

Astropy Collaboration et al., "Astropy: A community Python package for astronomy", A&A **558**, A33, A33 (2013).

Astropy Collaboration et al., "The Astropy Project: Building an Open-science Project and Status of the v2.0 Core Package", AJ **156**, 123, 123 (2018).

Behroozi, P. S. et al., "The Average Star Formation Histories of Galaxies in Dark Matter Halos from z = 0–8", ApJ **770**, 57, 57 (2013).

Belli, S. et al., "MOSFIRE Spectroscopy of Quiescent Galaxies at 1.5 < z < 2.5. II. Star Formation Histories and Galaxy Quenching", ApJ **874**, 17, 17 (2019).

[2] https://matplotlib.org/

[3] http://www.astropy.org

Benson, A. J. et al., "What Shapes the Luminosity Function of Galaxies?", ApJ **599**, 38 (2003).
Bertin, E. and S. Arnouts, "SExtractor: Software for source extraction.", A&AS **117**, 393 (1996).
Bisigello, L. et al., "The Impact of JWST Broadband Filter Choice on Photometric Redshift Estimation", ApJS **227**, 19, 19 (2016).
Brammer, G. B. et al., "EAZY: A Fast, Public Photometric Redshift Code", ApJ **686**, 1503 (2008).
Brodwin, M. et al., "The Era of Star Formation in Galaxy Clusters", ApJ **779**, 138, 138 (2013).
Calzetti, D. et al., "The Dust Content and Opacity of Actively Star-forming Galaxies", ApJ **533**, 682 (2000).
Carnall, A. C. et al., "Inferring the star formation histories of massive quiescent galaxies with BAGPIPES: evidence for multiple quenching mechanisms", MNRAS **480**, 4379 (2018).
Carnall, A. C. et al., "The VANDELS survey: the star-formation histories of massive quiescent galaxies at $1.0 < z < 1.3$", MNRAS **490**, 417 (2019).
Carnall, A. C. et al., "Timing the earliest quenching events with a robust sample of massive quiescent galaxies at $2 < z < 5$", MNRAS **496**, 695 (2020).
Carnall, A. C. et al., "How to Measure Galaxy Star Formation Histories. I. Parametric Models", ApJ **873**, 44, 44 (2019).
Cattaneo, A. et al., "The role of black holes in galaxy formation and evolution", Nature **460**, 213 (2009).
Cecchi, R. et al., "Quiescent Galaxies at $z \gtrsim 2.5$: Observations versus Models", ApJ **880**, L14, L14 (2019).
Davé, R. et al., "MUFASA: the assembly of the red sequence", MNRAS **471**, 1671 (2017).
Draine, B. T. and A. Li, "Infrared Emission from Interstellar Dust. IV. The Silicate-Graphite-PAH Model in the Post-Spitzer Era", ApJ **657**, 810 (2007).
Dunlop, J. S. et al., *PRIMER: Public Release IMaging for Extragalactic Research*, JWST Proposal. Cycle 1.
Ferland, G. J. et al., "The 2017 Release of Cloudy", Rev. Mexicana Astron. Astrofis. **53**, 385 (2017).
Fontana, A. et al., "The fraction of quiescent massive galaxies in the early Universe", A&A **501**, 15 (2009).
Forrest, B. et al., "An Extremely Massive Quiescent Galaxy at $z = 3.493$: Evidence of Insufficiently Rapid Quenching Mechanisms in Theoretical Models", ApJ **890**, L1, L1 (2020).

Galametz, A. et al., "CANDELS Multiwavelength Catalogs: Source Identification and Photometry in the CANDELS UKIDSS Ultra-deep Survey Field", ApJS **206**, 10, 10 (2013).

Girelli, G. et al., "Massive and old quiescent galaxies at high redshift", A&A **632**, A80, A80 (2019).

Hunter, J. D., "Matplotlib: a 2d graphics environment", Computing in Science & Engineering **9**, 90 (2007).

Ilbert, O. et al., "Accurate photometric redshifts for the CFHT legacy survey calibrated using the VIMOS VLT deep survey", A&A **457**, 841 (2006).

Ilbert, O. et al., "Mass assembly in quiescent and star-forming galaxies since $z \simeq 4$ from UltraVISTA", A&A **556**, A55, A55 (2013).

Kauffmann, O. B. et al., "Simulating JWST deep extragalactic imaging surveys and physical parameter recovery", A&A **640**, A67, A67 (2020).

Kereš, D. et al., "How do galaxies get their gas?", MNRAS **363**, 2 (2005).

Kroupa, P., "On the variation of the initial mass function", MNRAS **322**, 231 (2001).

Le Fèvre, O. et al., "The VIMOS Ultra Deep Survey: 10 000 Galaxies to Study the Early Phases of Galaxy Assembly at $2 < z < 6+$", The Messenger **155**, 37 (2014).

Leja, J. et al., "Beyond UVJ: More Efficient Selection of Quiescent Galaxies with Ultraviolet/Mid-infrared Fluxes", ApJ **880**, L9, L9 (2019).

Lilly, S. J. et al., "zCOSMOS: A Large VLT/VIMOS Redshift Survey Covering $0 < z < 3$ in the COSMOS Field", ApJS **172**, 70 (2007).

Marsan, Z. C. et al., "The Number Densities and Stellar Populations of Massive Galaxies at $3 < z < 6$: A Diverse, Rapidly Forming Population in the Early Universe", ApJ **924**, 25, 25 (2022).

McCracken, H. J. et al., "The COSMOS-WIRCam Near-Infrared Imaging Survey. I. BzK-Selected Passive and Star-Forming Galaxy Candidates at $z \gtrsim 1.4$", ApJ **708**, 202 (2010).

McCracken, H. J. et al., "UltraVISTA: a new ultra-deep near-infrared survey in COSMOS", A&A **544**, A156, A156 (2012).

Merlin, E. et al., "Chasing passive galaxies in the early Universe: a critical analysis in CANDELS GOODS-South", MNRAS **473**, 2098 (2018).

Muzzin, A. et al., "A Public K_s -selected Catalog in the COSMOS/ULTRAVISTA Field: Photometry, Photometric Redshifts, and Stellar Population Parameters", ApJS **206**, 8, 8 (2013).

Pacifici, C. et al., "The Evolution of Star Formation Histories of Quiescent Galaxies", ApJ **832**, 79, 79 (2016).

Peng, Y. et al., "Strangulation as the primary mechanism for shutting down star formation in galaxies", Nature **521**, 192 (2015).

Pozzetti, L. et al., "zCOSMOS - 10k-bright spectroscopic sample. The bimodality in the galaxy stellar mass function: exploring its evolution with redshift", A&A **523**, A13, A13 (2010).

Rieke, G. H. et al., "The Mid-Infrared Instrument for the James Webb Space Telescope, I: Introduction", PASP **127**, 584 (2015).

Rieke, M. J. et al., "Overview of James Webb Space Telescope and NIRCam's Role", in Cryogenic optical systems and instruments xi, Vol. 5904, edited by J. B. Heaney and L. G. Burriesci, Society of Photo-Optical Instrumentation Engineers (SPIE) Conference Series (2005), pp. 1–8.

Salim, S. et al., "Dust Attenuation Curves in the Local Universe: Demographics and New Laws for Star-forming Galaxies and High-redshift Analogs", ApJ **859**, 11, 11 (2018).

Schreiber, C. et al., "Near infrared spectroscopy and star-formation histories of 3 $\leq$ z $\leq$ 4 quiescent galaxies", A&A **618**, A85, A85 (2018).

Scoville, N. et al., "The Cosmic Evolution Survey (COSMOS): Overview", ApJS **172**, 1 (2007).

Straatman, C. M. S. et al., "The FourStar Galaxy Evolution Survey (ZFOURGE): Ultraviolet to Far-infrared Catalogs, Medium-bandwidth Photometric Redshifts with Improved Accuracy, Stellar Masses, and Confirmation of Quiescent Galaxies to z $\sim$ 3.5", ApJ **830**, 51, 51 (2016).

Valentino, F. et al., "Quiescent Galaxies 1.5 Billion Years after the Big Bang and Their Progenitors", ApJ **889**, 93, 93 (2020).

Weaver, J. R. et al., "COSMOS2020: A Panchromatic View of the Universe to $z \sim 10$ from Two Complementary Catalogs", ApJS **258**, 11, 11 (2022).

Wild, V. et al., "A new method for classifying galaxy SEDs from multiwavelength photometry", MNRAS **440**, 1880 (2014).

Williams, R. J. et al., "Detection of Quiescent Galaxies in a Bicolor Sequence from $z = 0-2$", ApJ **691**, 1879 (2009).

Wright, G. S. et al., "The Mid-Infrared Instrument for the James Webb Space Telescope, II: Design and Build", PASP **127**, 595 (2015).

Wu, P.-F. et al., "Star Formation Quenching in High-redshift Large-scale Structure: Post-starburst Galaxies in the Cl 1604 Supercluster at $z \sim 0.9$", ApJ **792**, 16, 16 (2014).

Wu, P.-F. et al., "Fast and Slow Paths to Quiescence: Ages and Sizes of 400 Quiescent Galaxies from the LEGA-C Survey", ApJ **868**, 37, 37 (2018).

Appendix A Complete Spectra List

The spectra are shown in Figures 14 to 16, alongside parameters of interest like the redshift posterior distribution, and χ^2 value. Cutouts, 10 arcseconds to a side,

are shown in Figures 17 to 19.

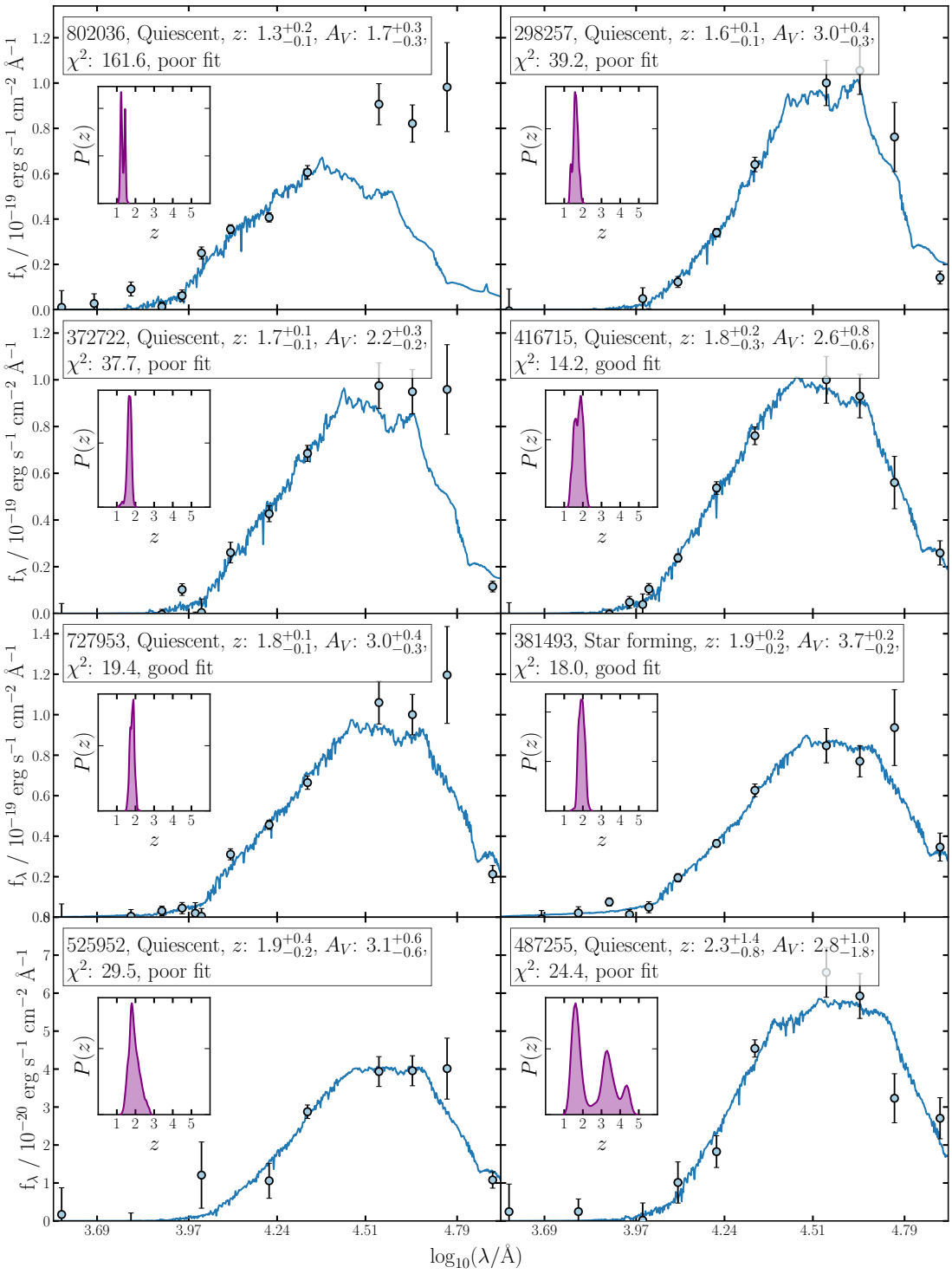

Figure 14: The 8 lowest redshift solutions for the 24 Quiescent galaxies identified in Section 2.

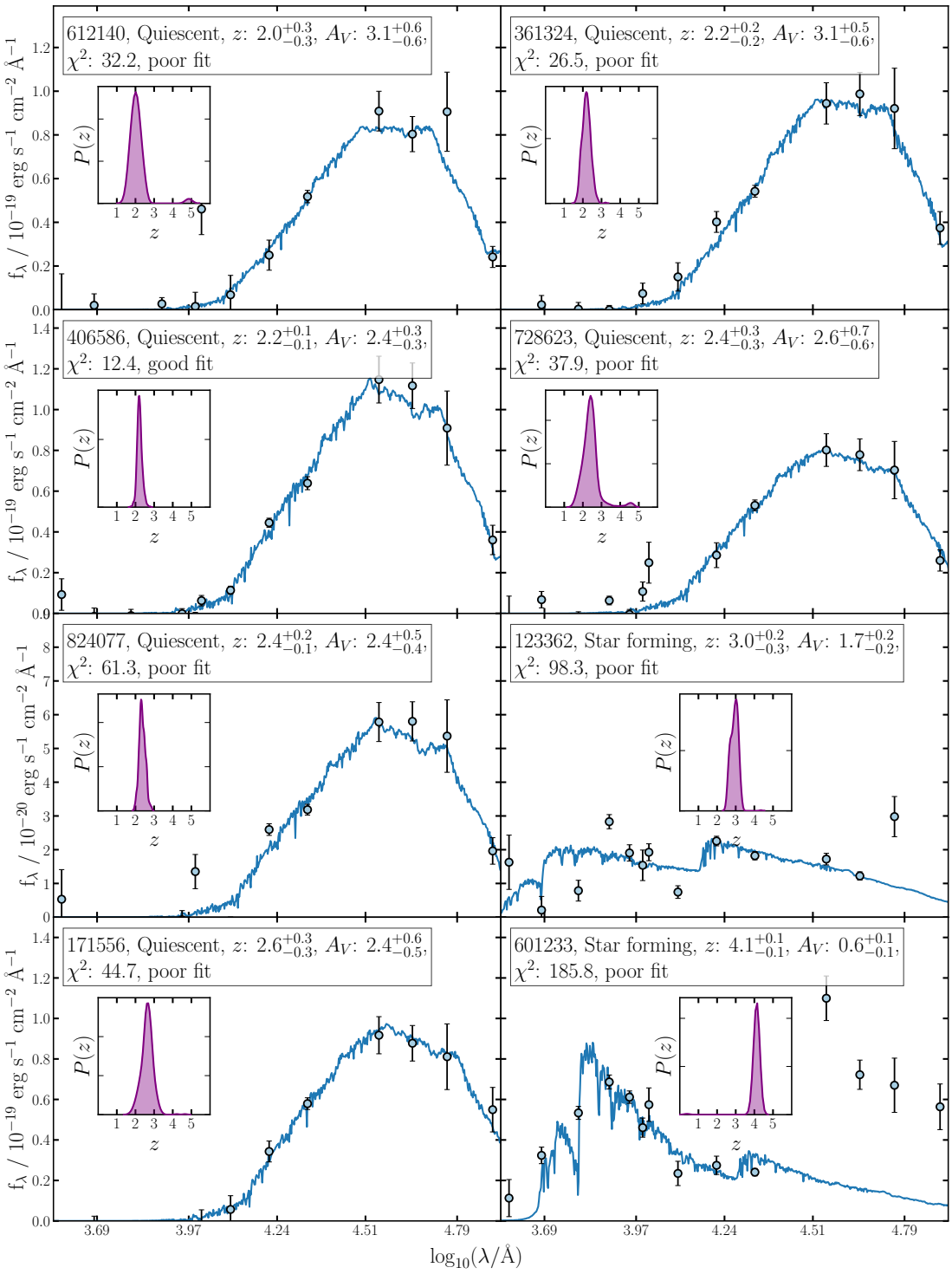

Figure 15: The 8 middle redshift solutions for the 24 Quiescent galaxies identified in Section 2.

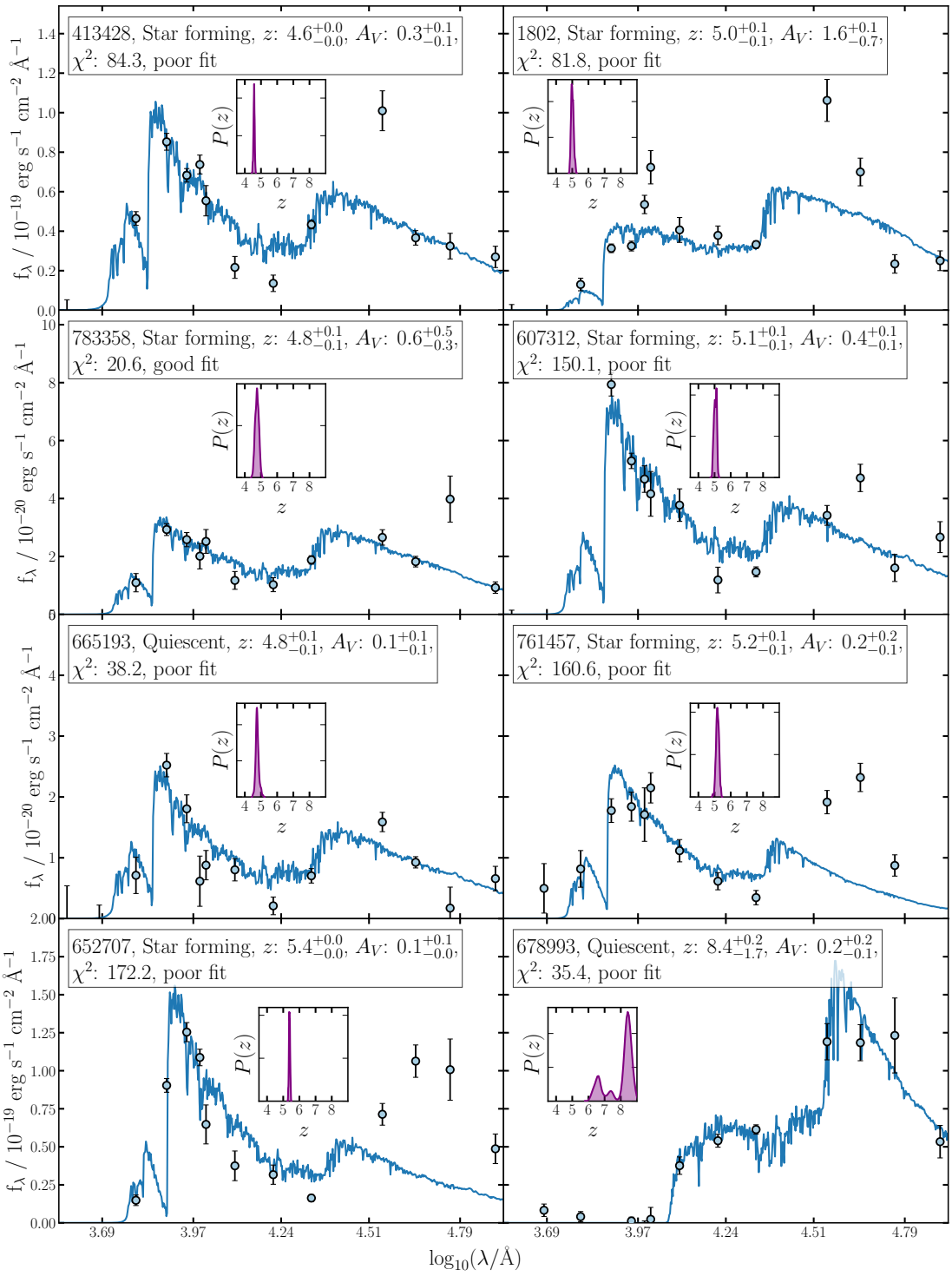

Figure 16: The 8 highest redshift solutions for the 24 Quiescent galaxies identified in Section 2.

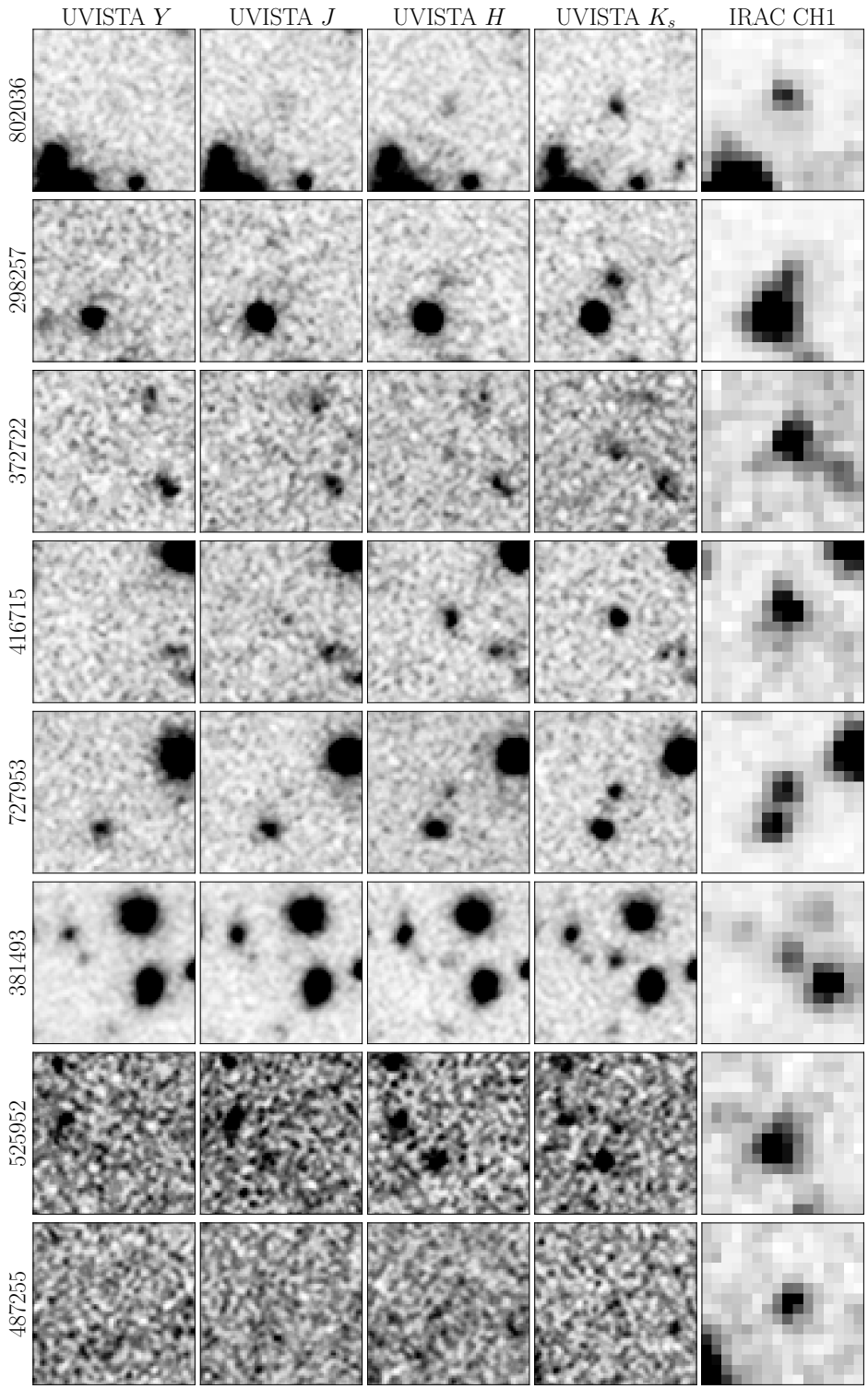

Figure 17: Cutouts of low redshift objects (Figure 14). Most objects have convincing Ks-band detections, and have little to no confusion.

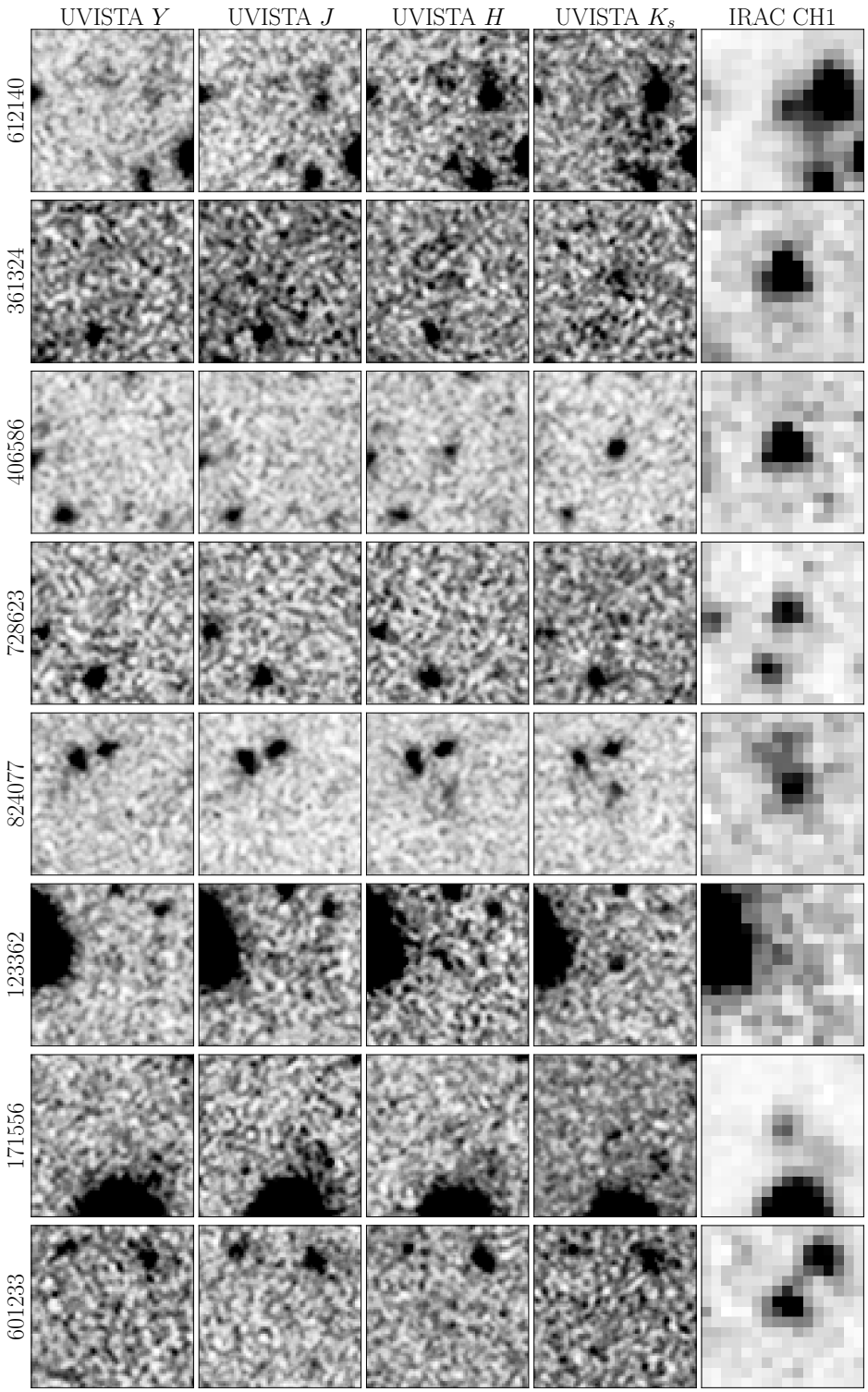

Figure 18: Cutouts of medium redshift objects (Figure 15). A mixture of good and bad detections.

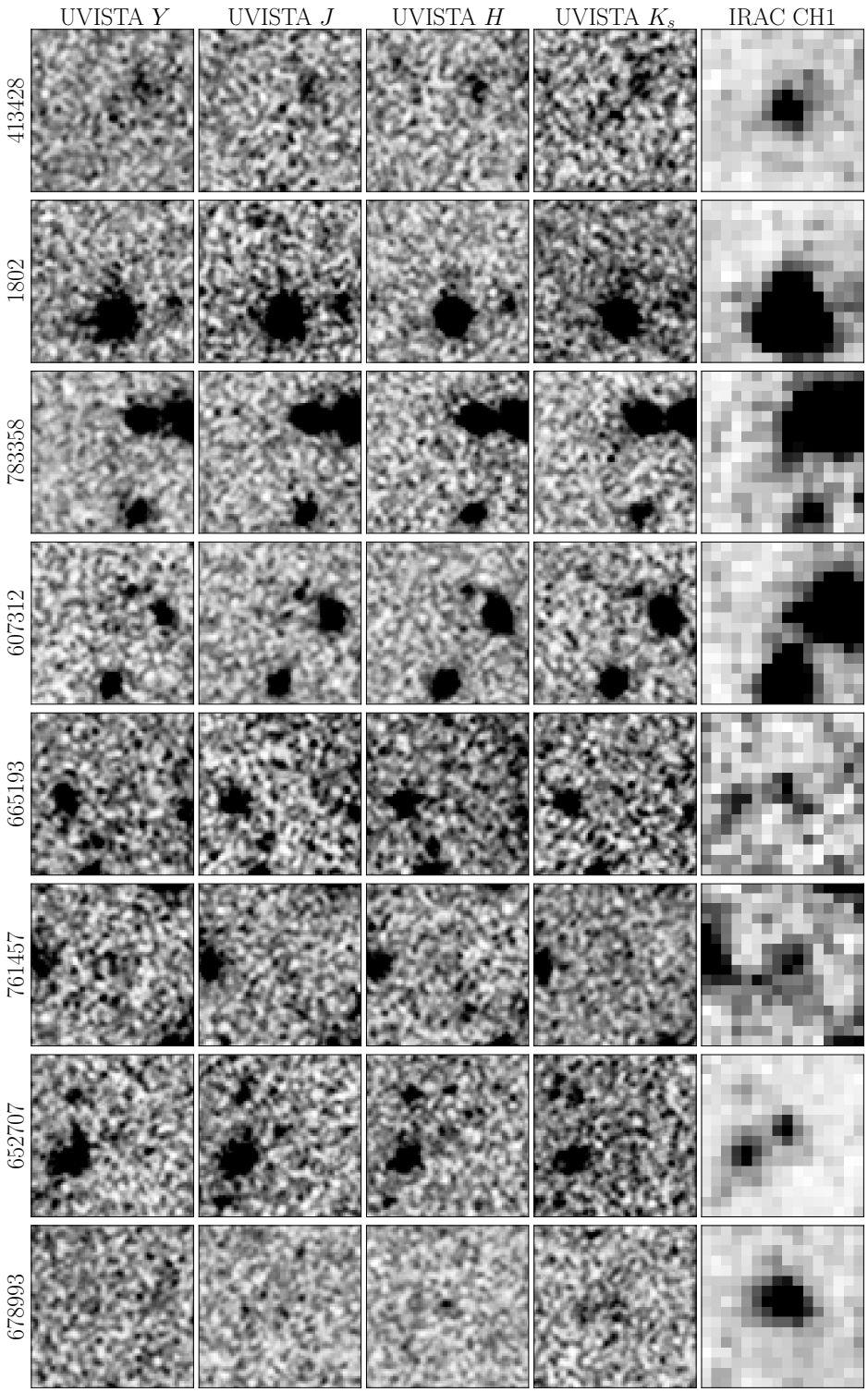

Figure 19: Cutouts of high redshift objects (Figure 16). No convincing detections and obvious confusion.